Reassessing the Effect of Cloud Type on Earth's Energy Balance in the Age of Active Spaceborne Observations. Part II: Atmospheric Heating

YUN HANG AND TRISTAN S. L'ECUYER

Department of Atmospheric and Oceanic Sciences, University of Wisconsin–Madison, Madison, Wisconsin

DAVID S. HENDERSON AND ALEXANDER V. MATUS

Space Science and Engineering Center, University of Wisconsin–Madison, Madison, Wisconsin

ZHIEN WANG

Department of Atmospheric and Oceanic Sciences and Laboratory for Atmospheric and Space Physics, University of Colorado Boulder, Boulder, Colorado

ABSTRACT

The role of clouds in modulating vertically integrated atmospheric heating is investigated using *CloudSat*'s multisensor radiative flux dataset. On the global mean, clouds are found to induce a net atmospheric heating of 0.07 ± 0.08 K day^{-1} that derives largely from 0.06 ± 0.07 K day^{-1} of enhanced shortwave absorption and a small, 0.01 ± 0.04 K day^{-1} reduction of longwave cooling. However, this small global average longwave effect results from the near cancellation of much larger regional warming by multilayered cloud systems in the tropics and cooling from stratocumulus clouds in subtropical oceans. Clouds are observed to warm the tropical atmosphere by 0.23 K day^{-1} and cool the polar atmosphere by -0.13 K day^{-1} enhancing required zonal heat redistribution by the meridional overturning circulation. Zonal asymmetries in the occurrence of multilayered clouds that are more frequent in the Northern Hemisphere and stratocumulus that occur more frequently over the southern oceans also leads to 3 times as much cloud heating in the Northern Hemisphere (0.1 K day^{-1}) than the Southern Hemisphere (0.04 K day^{-1}). These findings suggest that clouds very likely make the strongest contribution to the annual mean atmospheric energy imbalance between the hemispheres (2.0 ± 3.5 PW).

1. Introduction

Clouds play an important role in regulating Earth's energy balance (Stephens 2005) by modulating the amount of energy reflected, emitted, and absorbed at the surface and in the atmosphere (L'Ecuyer and Stephens 2003; Stephens et al. 2012a). The redistribution of energy within the atmosphere by clouds helps drive the large-scale circulation, vertical motions and the hydrological cycle (Webster and Stephens 1984; Ramanathan 1987; Chen et al. 2000; Stephens and Ellis 2008; Stephens et al. 2012a; Lin et al. 2013; Harrop and Hartmann 2016). The vertical distribution of radiative heating has been shown to be the primary way that clouds impact atmospheric circulations (Hartmann and Short 1980; Randall et al. 1989; McFarlane et al. 2007; Fueglistaler et al.

2009), the Madden–Julian oscillation (MJO), monsoons, and tropical rain belts (L'Ecuyer and Stephens 2003; Jiang et al. 2015; Johansson et al. 2015; Li et al. 2015; Winker et al. 2017). Although these studies suggest that the role of clouds in climate is significant, there are comparatively few observational constraints on how the vertical characteristics of clouds influence atmospheric heating and, in turn, affect global atmospheric energy transport. Yet there is evidence that climate models likely fail to quantitatively reproduce this influence (McFarlane et al. 2007; Cesana et al. 2019) since cloud heating depends critically on the vertical distributions of cloud properties, their frequency, and their environment, which are challenging to simulate accurately (Su et al. 2013; Zelinka et al. 2013; Jakub and Mayer 2015).

Quantifying the global energy budget has been a topic of intense renewed interest in recent years (Trenberth

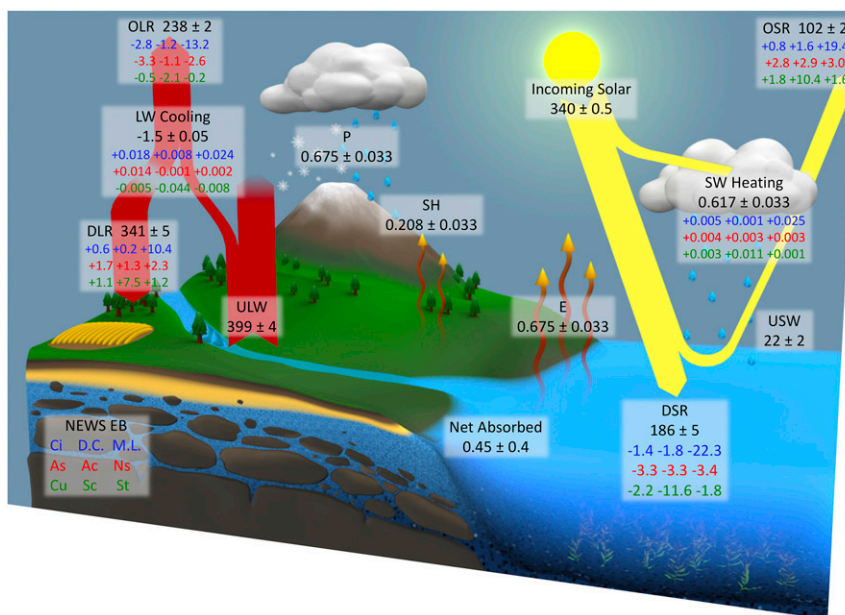*Corresponding author*: Yun Hang, yhang4@wisc.edu

FIG. 1. The observed annual mean global energy budget of Earth after applying relevant energy and water cycle balance constraints adapted from L'Ecuyer et al. (2015). The radiative effects of nine 2BCLD vertical cloud types are superimposed in colored text based on the results of Part I. All fluxes are reported in $W\,m^{-2}$ while heating due to precipitation P, evaporation E, sensible heating SH, and radiation (LW + SW) are reported in $K\,day^{-1}$. Heating rate in all subsequent figures are similarly reported in $K\,day^{-1}$ but can be converted to $W\,m^{-2}$ by multiplying by 120.

et al. 2009; Stephens et al. 2012b; L'Ecuyer et al. 2015; Stephens and L'Ecuyer 2015). The role of clouds in modulating energy balance has also been investigated through different approaches, such as examining cloud radiative effect characteristics of individual weather states (Oreopoulos and Rossow 2011), but revisiting the problem of distinguishing the roles of cloud types on atmospheric heating has received less attention. In the companion paper, L'Ecuyer et al. (2019, hereafter Part I) quantifies the contributions of nine unique cloud types, defined based on their vertical structure from *CloudSat* (Stephens et al. 2002) and *Cloud–Aerosol Lidar and Infrared Pathfinder Satellite Observation* (*CALIPSO*) (Winker et al. 2003), on top-of-atmosphere and surface radiation balance (Fig. 1). This combination of radar and lidar measurements provide a near-global view of the vertical structure of clouds, and allows direct observations of multilayered cloud systems, that are found to make the largest contribution to the energy budget (Sassen and Wang 2012; Part I). At the top-of-atmosphere (TOA), multilayered cloud systems reduce outgoing longwave radiation (OLR) by $13.2\,W\,m^{-2}$, and increase outgoing shortwave radiation (OSR) by $19.4\,W\,m^{-2}$, which accounts for about 20% of the total OSR. This runs contrary to classical cloud classifications

based on passive sensors in which many multilayered cloud types have traditionally been misclassified as midlevel clouds (Mace and Wrenn 2013; Part I).

CloudSat and *CALIPSO* also provide substantial improvements in cloud boundary information necessary to discern radiation at the surface. At the TOA, multilayered cloud systems enhance OSR by $19.4\,W\,m^{-2}$ and reduce downwelling shortwave radiation (DSR) at the surface by $22.3\,W\,m^{-2}$ (Part I). Part I also found that stratocumulus clouds strongly increase surface downwelling longwave radiation (DLR) by $7.5\,W\,m^{-2}$ and reduce TOA OLR by $2.1\,W\,m^{-2}$ suggesting that the greatest contribution to global atmospheric longwave (LW) cooling is from stratocumulus clouds ($-0.044\,K\,day^{-1}$) while multilayered clouds exert the greatest contribution to global atmospheric shortwave (SW) heating ($+0.025\,K\,day^{-1}$). These results provide valuable constraints on TOA and surface energy balance and hint at the different roles distinct cloud types may play in atmospheric heating; however, clouds with similar TOA radiative signatures can have impacts on atmospheric heating in the atmosphere and exert very distinct influences on large scale circulations (Mace and Wrenn 2013). To help address this issue, this work extends the analysis described in Part I to examine the

influence of cloud morphology on the spatial distribution of heating within the atmosphere.

The earliest efforts to quantify radiative heating in the atmosphere began in the mid-twentieth century (Manabe and Möller 1961; Manabe and Strickler 1964; Manabe and Wetherald 1967). After entering the satellite era in the 1960s, observations from passive sensors on polar-orbiting satellites revolutionized our understanding of the global top-of-atmosphere radiative fluxes and, through radiative transfer calculations, atmospheric heating in the next several decades (Sabatini and Suomi 1962; Vonder Haar and Suomi 1971; Hartmann and Short 1980; Rossow and Zhang 1995; Wielicki et al. 1996; Zhang et al. 2004; Kato et al. 2005). More recently, ground-based active sensors and field campaigns have provided high-quality estimates of the vertical structure of radiative heating in the atmosphere at fixed locations (Johnson and Young 1983; McFarlane et al. 2007) but extrapolating this information to global scales was challenging until the launch of the *CloudSat* and *CALIPSO* in 2006 (Stephens et al. 2002; Winker et al. 2007; Stephens et al. 2008; Oreopoulos et al. 2017). Previous work from Haynes et al. (2013) demonstrated that the active *CloudSat* and *CALIPSO* sensors provide the only means for examining profiles of atmospheric heating from space. When integrated vertically, such observations can be used to document the spatial distribution of cloud impacts on radiative heating in the atmosphere. Building on Part I, this study quantifies the impacts of nine distinct cloud types, defined based explicitly by their vertical structure, on column atmospheric heating.

The paper is organized as follows. Section 2 describes each dataset and the methods used in this analysis. Section 3 discusses the cloud impact on column-integrated atmospheric heating and illustrates the dramatically different characteristics of the heating under distinct cloud types. After that, the effects of clouds on atmospheric radiative heating are further explored by their vertical structures. Finally, summary and discussion are provided in section 4.

2. Datasets

a. *CloudSat's 2B-CLDCLASS-lidar data product*

Understanding cloud influences on atmospheric heating is challenging for passive sensors due to their limitations in detecting cloud vertical structure. Previous cloud classifications such as the International Satellite Cloud Climatology Project (ISCCP) (Rossow and Schiffer 1999) have led to important breakthroughs in understanding cloud effects. However, ISCCP classifies cloud types based on cloud-top pressure and optical depth, which leads to ambiguity in multilayered and thin cloud scenarios and provides limited information concerning cloud-base height (Mace et al. 2006; Marchand et al. 2010; Mace and Wrenn 2013). Errors in cloud-base height can, in turn, cause significant errors in the surface flux estimates required to compute column atmospheric heating (Henderson et al. 2013; Mülmenstädt et al. 2018). Fortunately, these barriers can be sufficiently overcome by the spaceborne active sensors that form the basis for *CloudSat*'s level 2 cloud scenario classification (2B-CLDCLASS-lidar, hereafter 2BCLD) and radiative flux and heating rate (2B-FLXHR-lidar, hereafter 2BFLX) products. 2BCLD utilizes synergistic observations from *CloudSat*, *CALIPSO*, and Moderate Resolution Imaging Spectroradiometer (MODIS) (Platnick et al. 2003) to characterize cloud type based on explicit vertical structure information (Stephens et al. 2002; Sassen et al. 2008; L'Ecuyer and Jiang 2010). *CloudSat*'s 94 GHz Cloud Profiling Radar (CPR) radar is capable of resolving the vertical structure of clouds with a resolution of 240 m (Tanelli et al. 2008). *CALIPSO*'s Cloud–Aerosol Lidar with Orthogonal Polarization (CALIOP) lidar can detect subvisual cirrus and low-lying liquid clouds that go undetected by the CPR (McGill et al. 2007; Winker et al. 2007). Together, these sensors provide the most accurate depiction of the vertical distribution of clouds currently available (Mace et al. 2009). In addition, MODIS provides complementary measurements of cloud effective radius and integrated optical thickness that further constrain cloud radiative properties (Chan and Comiso 2011).

The 2BCLD product groups all single-layered cloud scenes observed by *CloudSat* and *CALIPSO* into eight types: stratus (St), stratocumulus (Sc), cumulus (Cu), nimbostratus (Ns), altocumulus (Ac), altostratus (As), deep convective (D.C.), and cirrus (Ci) clouds (Sassen and Wang 2008). The most notable innovation 2BCLD offers, however, is being able to further identify multilayered (M.L.) cloud systems, which are defined as scenes containing more than one cloud type identified in multiple distinct layers separated by at least one full 240 m range bin. In fact, 2BCLD indicates that 29.9% of the globe is characterized by cloudy scenes containing more than one cloud layer as evidenced by Fig. 2 that shows the annual mean frequencies of all eight *CloudSat*/*CALIPSO* cloud types and M.L. clouds adopted in this study (Part I). Low-level clouds, especially single-layered stratocumulus also have large global occurrence (15.5%) and are prevalent over midlatitude oceans and subtropical eastern ocean margins. High-level clouds are
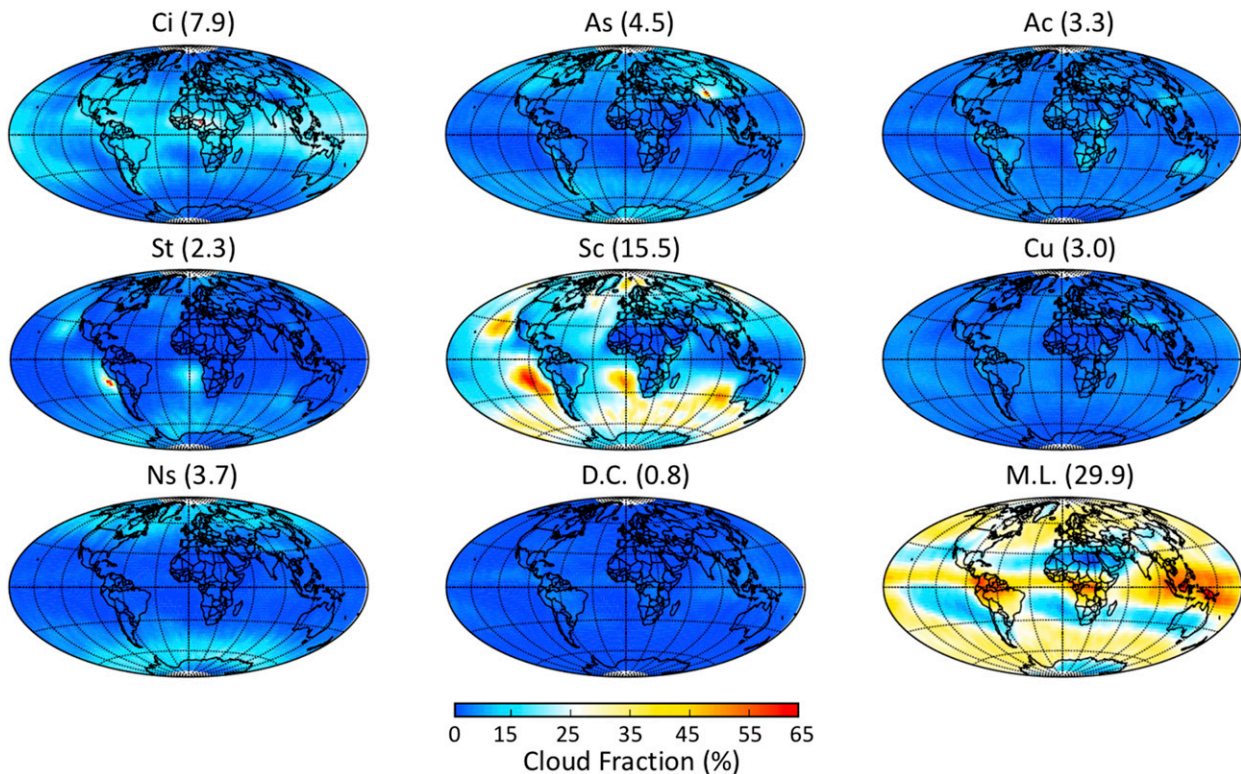
FIG. 2. Annual mean cloud fraction (%) according to cloud type determined based on the 2BCLD classification, 2007–10 (reproduced from Part I for completeness). Global averages are shown in parentheses. Ci = cirrus, As = altostratus, Ac = altocumulus, St = stratus, Sc = stratocumulus, Cu = cumulus, Ns = nimbostratus, D.C. = deep convection, and M.L. = multilayered cloud system.

most frequently observed near the equator and over tropical continents. Midlevel clouds, such as altostratus and nimbostratus clouds, are predominate over high latitudes.

Figure 3 illustrates the cloud types that make up the most and the second most frequent top and bottom layers in multilayered cloud pixels. The most frequent bottom layers are altocumulus over the land and stratocumulus over the ocean. Globally, the most frequent top layer is cirrus; the second most frequent top layers are altocumulus over subtropical oceans and altostratus over tropical land and midlatitude oceans. Over the southern oceans, altostratus is the most frequent top layer and cirrus is the second frequent top layer. Figure 4 further shows the frequency of single-layered and different types of multilayered clouds. In the tropics, two-layered clouds make up nearly 40% of the total cloud fraction, are found to be as important as the single-layered clouds. Three-layered clouds make up 15% in the tropical regions.

b. CloudSat's 2B-FLXHR-lidar data product

2BFLX is used to assign radiative properties to each cloud scene. 2BFLX produces estimates of broadband

fluxes consistent with observations from *CloudSat*, *CALIPSO*, and MODIS (L'Ecuyer et al. 2008; Henderson et al. 2013; Matus and L'Ecuyer 2017). For each vertical profile from *CloudSat*, fluxes and heating rates are computed at a vertical resolution of 240 m using the BUGSrad broadband radiative flux model (Ritter and Geleyn 1992). Liquid and ice cloud effective radii and water contents utilized in 2BFLX derive from *CloudSat*'s Level-2 cloud water content product (Austin 2007; Austin et al. 2009) and the *CloudSat* 2C-ICE product (Deng et al. 2013). Ancillary temperature and humidity profiles are provided by European Centre for Medium-Range Weather Forecasts (ECMWF) analyses. Spectral surface albedo and emissivity are assigned using the International Geosphere–Biosphere Programme (IGBP) global land surface classification (Henderson et al. 2013) supplemented by ancillary snow and sea ice measurements from the Advanced Microwave Scanning Radiometer for Earth Observing System (EOS) (AMSR-E). As described below, the retrieval also implements surface characteristics derived by other satellite and field campaign studies.

This study utilizes the fifth release (R05) 2BFLX, which incorporates significant improvements compared
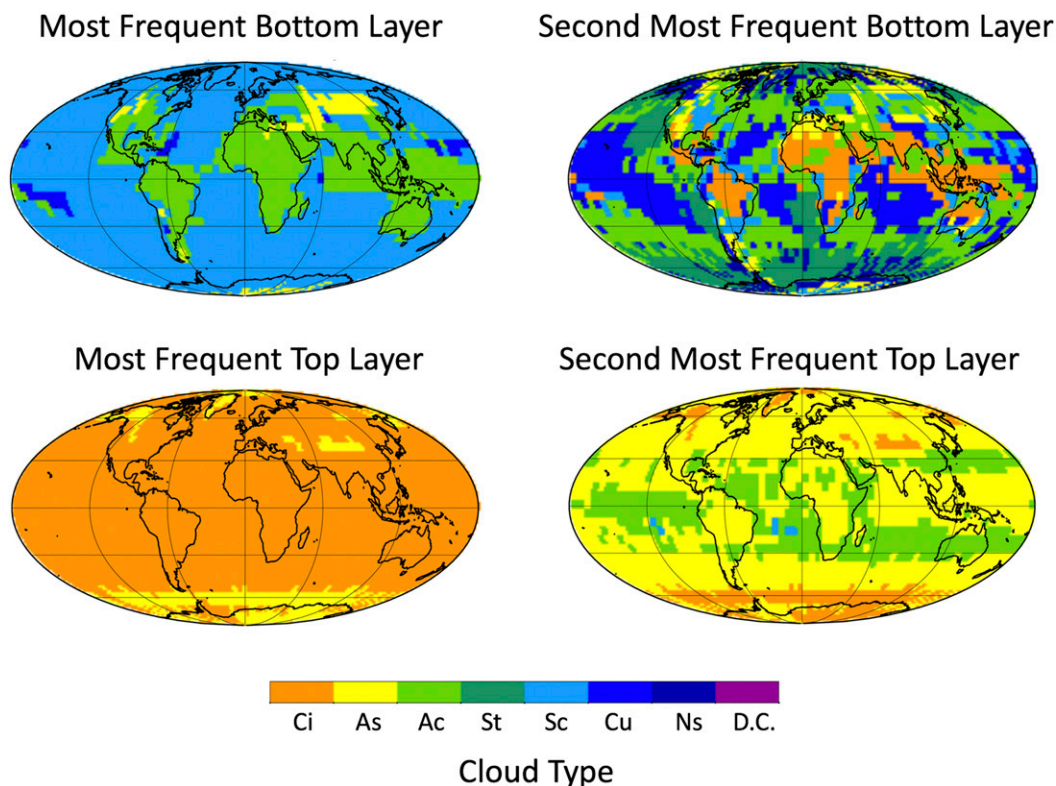
FIG. 3. The most frequent and the second frequent cloud types identified as the bottom and top layers of multilayered clouds.

with the previous version (Henderson et al. 2013). A majority of the changes in the R05 retrieval are outlined in Matus and L'Ecuyer (2017). The R05 2BFLX imparts heavy emphasis on providing more realistic representations of cloud and surface characteristics including land, snow, and sea ice albedos from Zatko and Warren (2015) and ocean surface albedo following Jin et al. (2011). Further, land emissivities in the LW are now spectrally resolved for multiple surface types in IGBP using emissivity values from Huang et al. (2016). Improved cloud and aerosol detection are implemented through the use of *CALIPSO*, version 4, cloud and aerosol datasets, IWC and effective radii in cirrus clouds derived from 2C-ICE, and explicit representation of mixed-phase clouds using the 2B-CLDCLASS-lidar phase discrimination (Van Tricht et al. 2016). These improvements significantly impact radiative fluxes (Henderson et al. (2013); Tables 6 and 7) resulting in reduced error when compared to validation sources (e.g., Matus and L'Ecuyer (2017); McIlhattan et al. (2017)).

As discussed in Matus and L'Ecuyer (2017), 2BFLX global and regional fluxes yield good agreement when evaluated against the Clouds and the Earth's Radiant Energy System (CERES) single scanner footprint (SSF)

fluxes reported in the *CALIPSO*, *CloudSat*, CERES, and MODIS (CCCM) product (Kato et al. 2010). Matus and L'Ecuyer (2017) found that biases in land and ocean surface reflectance are reduced globally by over 40% in clear-sky scenes. Further, the all-sky bias is reduced due to improvements in the representation of mixed-phase and thin cirrus clouds. In particular, the inclusion of mixed-phase clouds reduces biases over the Southern Ocean, which play an important role in hemispheric energy imbalance (discussed further in section 3c). Overall, clear-sky fluxes exhibit good agreement between 2BFLX and CERES with a net bias and RMSE of less than −0.9% and 2.8% in net fluxes at 2.5° × 2.5° spatial and monthly temporal resolution, respectively. Biases and RMSE increase in cloudy scenes, largely due to the different scanner footprint sizes between CERES and *CloudSat*/*CALIPSO*; the level of agreement in SW and LW fluxes also varies by individual cloud types.

Like other spaceborne platforms, there are some ambiguities associated with interpreting *CloudSat* and *CALIPSO* observations owing to aerosols and sensitivity limitations. Some multilayered clouds may be missed, especially in the tropics, due to the CPR ground-clutter issues and attenuation of the lidar (Protat et al. 2014). Further, LW radiation is sensitive to the assumed
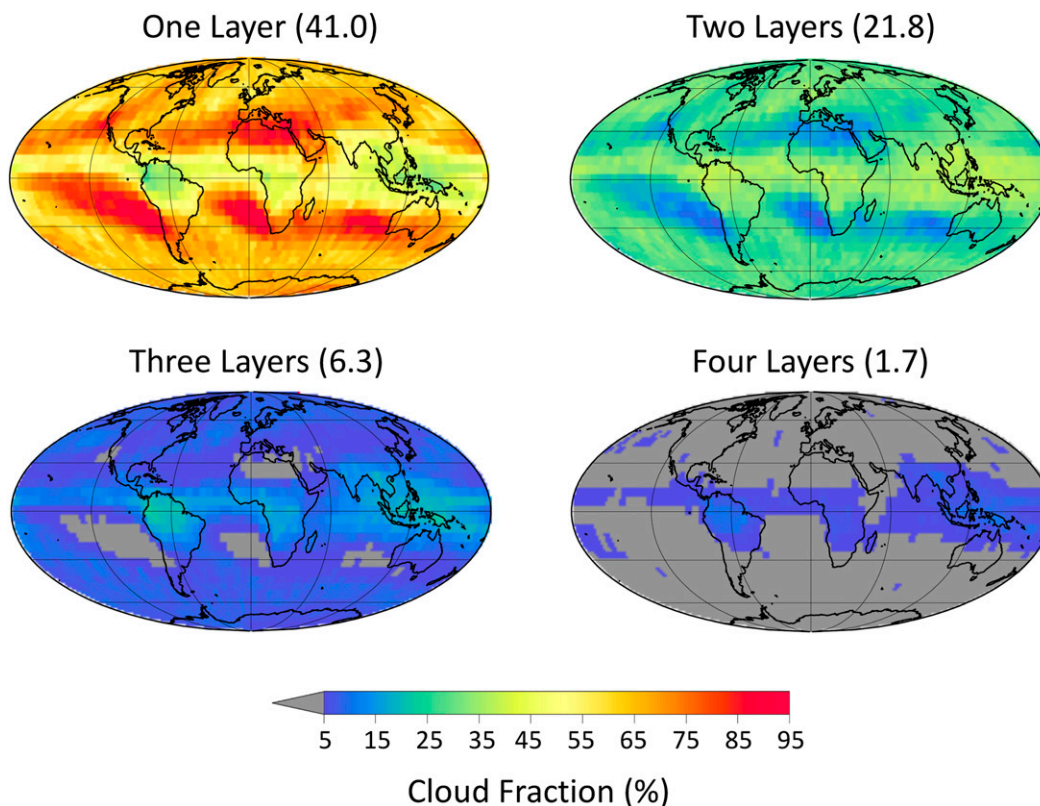
FIG. 4. The frequency of single-layered and multilayered clouds (%). The multilayered clouds are classified as two layers, three layers, and four layers.

temperature profile, but 2BFLX utilizes coincident ECMWF analyses at the 0130 and 1330 local overpass times, neglecting other times during the diurnal cycle (Cesana et al. 2019; L'Ecuyer et al. 2008). Similarly, 2BCLD only samples clouds at these local times resulting in a limited representation of the diurnal cycle of cloud cover.

c. Analysis methods

This study uses 2BCLD and 2BFLX to investigate the impact of clouds on column-integrated atmospheric heating. The atmospheric heating rate Q is defined as

$$Q(p) = \frac{dT}{dt} = -\frac{g}{c_p}\frac{\Delta F_{net}}{\Delta p} = -\frac{g}{c_p}\frac{\Delta F^{\downarrow} - \Delta F^{\uparrow}}{\Delta p} \quad (1)$$

where T is temperature, t is time, g is the gravitational constant, c_p is the specific heat capacity of dry air, F_{net} is net radiative flux defined as the difference between downward and upward fluxes, and p is pressure. 2BFLX applies Eq. (1) to LW and SW flux profiles at the full *CloudSat* vertical resolution to derive vertical profiles of atmospheric radiative heating in all-sky conditions. A separate set of broadband flux calculations are derived

for each *CloudSat* profile with all condensate removed to establish clear-sky heating rates from which cloud impacts can be derived. The column-integrated heating is computed by evaluating Eq. (1) between the top of the atmosphere and the surface. The cloud impact on atmospheric heating Q_{cld} can then be derived as the difference in heating rates between clear-sky and all-sky conditions. It is straight-forward to show that this is equivalent to differencing the TOA and surface cloud radiative effect (CRE), which were examined in Part I:

$$
\begin{aligned}
Q_{cld} = Q_{all} - Q_{clr} = &\frac{g}{c_p \Delta p}\{[(F_{toa}^{\downarrow} - F_{sfc}^{\downarrow}) - (F_{toa}^{\uparrow} - F_{sfc}^{\uparrow})]_{all} \\
&- [(F_{toa}^{\downarrow} - F_{sfc}^{\downarrow}) - (F_{toa}^{\uparrow} - F_{sfc}^{\uparrow})]_{clr}\} \\
= &\frac{g}{c_p \Delta p}\{[(F_{toa}^{\downarrow} - F_{toa}^{\uparrow})_{all} - (F_{toa}^{\downarrow} - F_{toa}^{\uparrow})_{clear}] \\
&- [(F_{sfc}^{\downarrow} - F_{sfc}^{\uparrow})_{all} - (F_{sfc}^{\downarrow} - F_{sfc}^{\uparrow})_{clr}]\} \\
= &\frac{g}{c_p \Delta p}(CRE_{toa} - CRE_{sfc}) \quad (2)
\end{aligned}
$$

This calculation yields the values reported in the SW heating and LW cooling boxes in Fig. 1. This study investigates the impact of clouds on atmospheric heating using data from the preanomaly phase of the *CloudSat*

mission from January 2007 to December 2010 that provided near-global daytime and nighttime coverage from 82.5°S to 82.5°N. All data are gridded to 2.5° × 2.5° spatial resolution to ensure adequate sampling on monthly time scales. Since *CloudSat* and *CALIPSO* measurements are always collected at 01:30 and 13:30 local time, the estimated SW fluxes are normalized to the diurnally averaged insolation to approximate the full diurnal cycle. It should be noted, however, that this does not account for diurnal variations in cloud cover other than those directly observed at the two sampling times at 0130 and 1330 local time.

d. GPCP-WALRUS data product

To place the cloud impacts derived here in the context of the other main drivers of atmospheric heating, they are compared against clear-sky radiative cooling estimates from 2BFLX and estimates of column-integrated latent heat. Latent heat release from precipitation is estimated primarily using observations from the Global Precipitation Climatology Project (GPCP) augmented in warm rain regions using the *CloudSat*-based Wisconsin Algorithm for Latent Heat and Rainfall Using Satellites (WALRUS) (Nelson et al. 2016). GPCP provides global, monthly rainfall estimates at 2.5° × 2.5° resolution derived from merged polar-orbiting and geosynchronous satellite from 1997 to present under the World Climate Research Programme (Huffman et al. 1997). These rainfall estimates include all forms of precipitation but may miss some isolated warm rain in subsidence regions. To account for this small additional source of latent heating, GPCP observations are augmented using WALRUS latent heat estimates in areas where the latter observes more rainfall following the method described in Nelson and L'Ecuyer (2018). WALRUS uses a Bayesian Monte Carlo methodology that couples cloud-resolving model simulations from the Regional Atmospheric Modeling System (RAMS) (Saleeby and Cotton 2004; Saleeby and van den Heever 2013) to *CloudSat* observations to retrieve latent heat profiles at *CloudSat*'s 1.5-km spatial and 240 m vertical resolution (Nelson and L'Ecuyer 2018). GPCP and WALRUS data from the period of 2007–10 are adopted to be consistent with the radiative heating estimates.

3. Results

a. Global distribution of cloud impact on atmospheric heating

Cloud impacts on column-integrated atmospheric net, SW, and LW radiative heating are shown in Fig. 5. Averaged globally, clouds produce a net planetary

atmospheric heating of $0.07 \pm 0.08 \, \text{K day}^{-1}$, increasing SW absorption by $0.06 \pm 0.07 \, \text{K day}^{-1}$ and LW heating by only $0.01 \pm 0.04 \, \text{K day}^{-1}$. Error bounds are derived using the same methodology in Part I and are defined using discrepancies between 2BFLX and CERES TOA fluxes, as well as possible shortcomings in the 2BFLX retrieval. The CERES instrument aboard *Aqua* provides a unique opportunity for evaluating 2BFLX, because of the small temporal gap between the orbits of *Aqua* satellite and *CloudSat*. Using the CERES TOA fluxes as a reference, uncertainties in TOA fluxes are derived based on the biases between 2BFLX and CERES presented in Matus and L'Ecuyer (2017) for SW and LW fluxes. At the surface, sensitivity studies presented in Henderson et al. (2013) suggest that the largest uncertainties 2BFLX surface flux estimates derive from *CloudSat* liquid water content, surface temperature, and lower-troposphere humidity. Further, significant regional errors in downwelling LW fluxes may arise due to uncertainty in cloud-base heights (Mülmenstädt et al. 2018). The total uncertainty at the surface is derived by summing the square of the uncertainties listed in the aforementioned sensitivity analyses and taking the square root of the resultant sum. The overall column integrated net, SW, and LW error bounds are then calculated following Eq. (2) using the resultant total TOA and surface uncertainty estimates. Since the cloud impact on atmospheric heating is computed as the difference between two large numbers each with nonnegligible uncertainties, errors in cloud impacts on top-of-atmosphere and surface fluxes are amplified in atmospheric heating leading to much larger fractional uncertainties.

Despite their relatively small global effects, however, the distinct vertical structures of clouds in different regions leads to substantial variations in LW heating that produce large (primarily zonal) variations in cloud heating (Haynes et al. 2013; Li et al. 2016). Regionally, LW heating ranges from $0.5 \, \text{K day}^{-1}$ in the tropical warm pool and a minimum cooling of $-0.2 \, \text{K day}^{-1}$ over the subtropical oceans. Clouds do not enhance much total column SW absorption compared to LW. Enhancement within cloud is apparently partially compensated by reduced water vapor absorption below the cloud (Oreopoulos et al. 2016). This is especially true over the darker oceans but clouds are observed to enhance SW atmospheric warming over higher albedo land surfaces where they interact with both incoming and reflected radiation. Thus while SW heating over land surfaces is almost entirely responsible for the global mean cloud heating, the large regional variability in LW heating dominates its spatial distribution. It is clearly shown in the observed zonal distribution of cloud
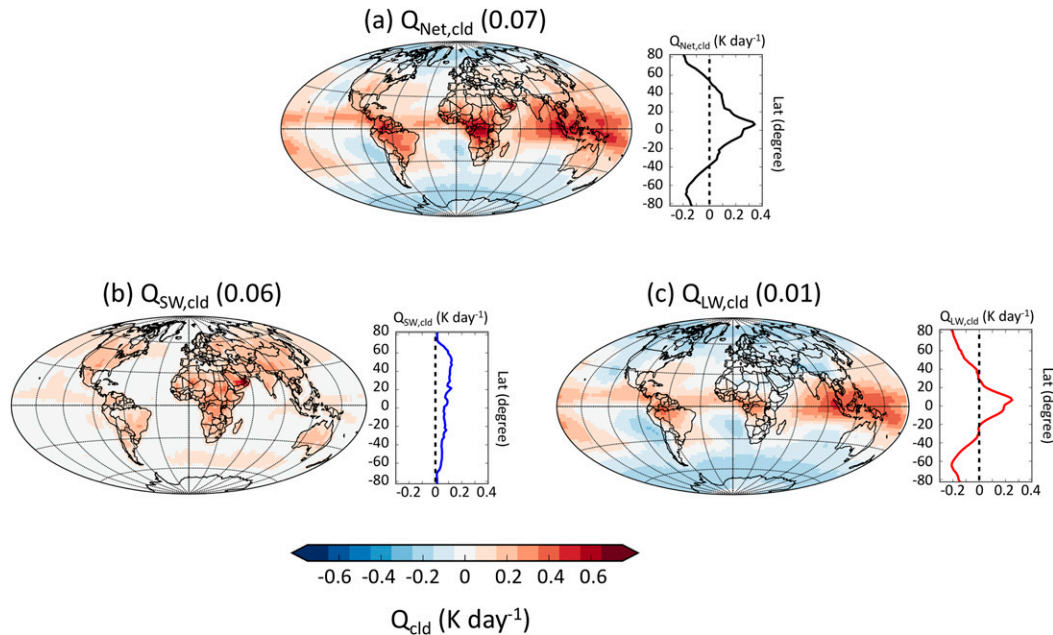
FIG. 5. Annual mean cloud impact on column-integrated (a) net, (b) SW, and (c) LW atmospheric radiative heating ($K\ day^{-1}$). The global average is shown in parentheses. Zonal averages are shown on the right.

impacts on atmospheric heating that imply that clouds exert a strong influence on large-scale meridional circulations, enhancing equator to pole energy gradients by radiatively warming the tropics and cooling higher latitudes. This requires an increased rate of meridional energy transport in the atmosphere relative to the initial clear-sky radiative cooling imbalances that control the underlying circulation on a global scale (Sohn and Smith 1992; Soden and Held 2006). Recent comparisons with climate models have shown that cloud influences on heating is underestimated in convective regimes, while the impact on cooling is underestimated in subsidence regimes because models tend to simulate fewer low clouds (Cesana et al. 2019).

Figure 6 decomposes the cloud impact on annual mean column-integrated net atmospheric heating into the contributions from each of the nine *CloudSat*/*CALIPSO* cloud types shown in Fig. 2. By far the most striking feature in Fig. 6 is the strong contribution from multilayered clouds that bears a strong resemblance to the total $Q_{Net,cld}$ (Fig. 5). For example, the active sensors aboard *CloudSat* and *CALIPSO* demonstrate that multilayered cloud systems contribute more than 2.5 times at much global heating as single-layer cirrus clouds. This indicates the fact that cirrus make up the top layer in the vast majority of multilayered clouds, but active sensors suggest that a majority of cirrus cloud radiative effects derive from multilayered cloud scenes rather than single-layer cirrus (Fig. 2). In some regions such as equatorial Africa, the Sahel, and the tropical

warm pool, multilayered clouds warm the atmosphere by more than $0.24\ K\ day^{-1}$. Conversely, low cloud types are found to enhance atmospheric radiative cooling. Stratocumulus clouds, in particular, cool the atmosphere by $-0.03\ K\ day^{-1}$. Over subtropical subsidence regions, the cooling introduced by Peruvian stratocumulus clouds exceeds $-0.16\ K\ day^{-1}$. The other major Sc regions off the west coasts of California, Namibia, Australia, and the Canary Islands cool the atmosphere by about $-0.12\ K\ day^{-1}$. Nimbostratus and altostratus clouds tend to exert a small influence on net atmospheric radiative heating owing to a local cancellation of SW warming and LW cooling effects, even though they are observed somewhat more frequently in the Northern Hemisphere (NH) (Fig. 2).

Decomposing cloud impacts on atmospheric heating into SW (Fig. 7) and LW (Fig. 8) components provides additional insights into the heat budget of the atmosphere. Globally, multilayered cloud systems are found to increase SW atmospheric heating by $0.03\ K\ day^{-1}$ but exert much larger influences over land regions. The largest impacts are observed in equatorial Africa, the Sahel, and Southeast Asia where SW heating from multilayered clouds exceeds $0.12\ K\ day^{-1}$. Cirrus and altostratus clouds exhibit smaller but still significant enhanced SW warming over the Sahel and Western China, respectively.

As noted above, however, the distribution of cloud influences on net atmospheric heating is dominated by the cloud impacts on LW heating. Figure 8 suggests that
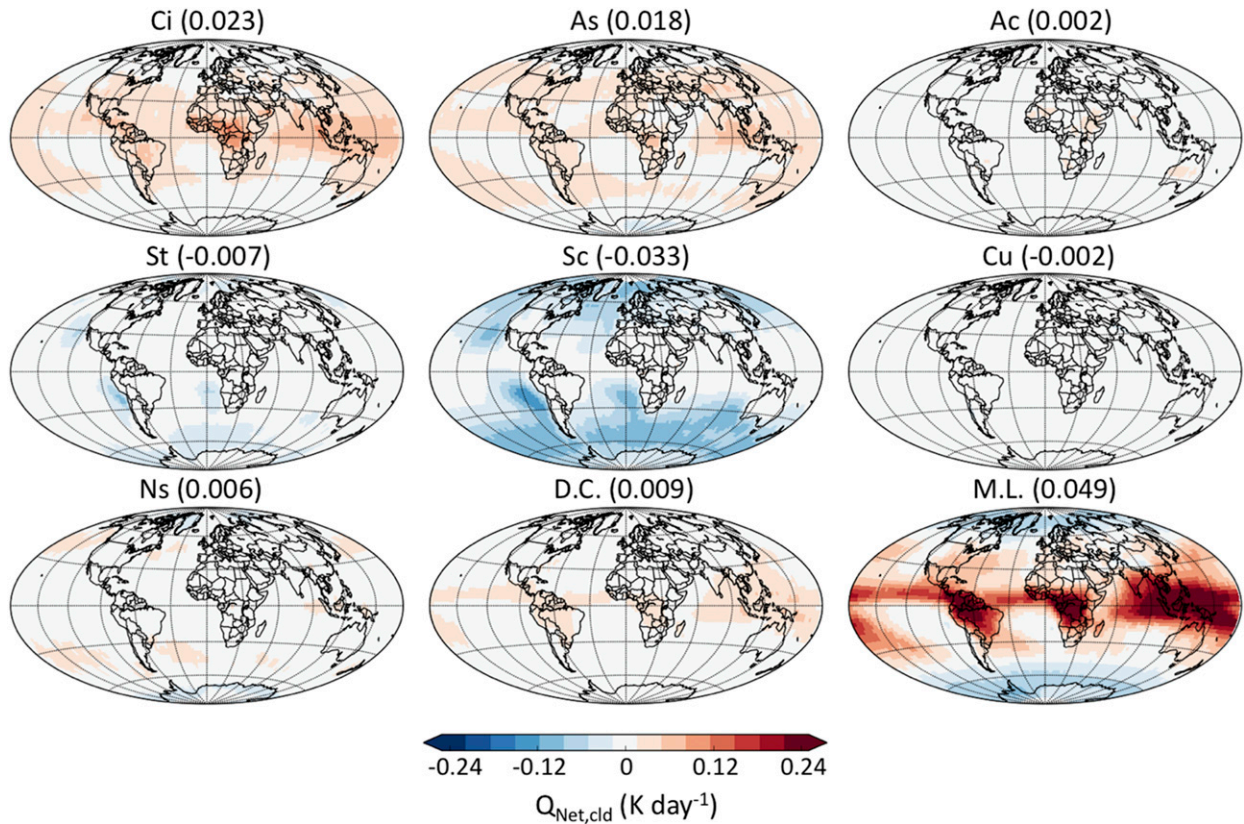
FIG. 6. Annual mean cloud impact on column-integrated atmospheric net radiative heating (K day^{-1}). Cloud types are determined based on 2B-CLDCLASS-lidar cloud classification. Global average is shown in parentheses.

the global pattern of atmospheric LW radiative heating from clouds results primarily from the sum of two cloud types: M.L. and stratocumulus clouds. A predominant warming from multilayered cloud systems is modulated in subsidence regions and over the southern oceans by enhanced cooling from marine stratocumulus. Multilayered cloud systems act to substantially enhance the LW heating over intertropical convergence zone (ITCZ), while stratocumulus clouds act to enhance the LW cooling over midlatitude oceans.

b. *Role of cloud type in defining meridional heating gradients*

Figure 1 suggests that the net cloud impact on global mean atmospheric radiative heating is small, compared to latent heating and sensible heating. However, as shown in Fig. 5, clouds significantly influence meridional gradients in atmospheric heating. This is further emphasized in Fig. 9 that displays the annual mean impact of each cloud type on zonal–annual mean atmospheric radiative heating. Clouds significantly enhance tropical atmospheric heating maximizing at 7°N with the majority of heating contributed by cirrus and

multilayered clouds. Clouds also substantially cool the atmosphere at high latitudes owing to cooling from stratocumulus and multilayered clouds. This result is consistent with Chen et al. (2000) who clearly showed the enhancement of the meridional gradient in atmospheric heating by clouds, but midlevel clouds contributed more cooling effects at high latitudes. One reason for the discrepancy may be that the multilayered clouds containing a combination of high and low cloud are misinterpreted as midlevel clouds by passive sensors (Mace et al. 2009; Marchand et al. 2010; Mace and Wrenn 2013).

To understand the significance of these impacts, the magnitudes of these effects are placed in the context of total atmospheric heating, Q_{atm}, defined as

$$Q_{atm} = f_{clr}(\langle Q_{SW,clr} \rangle + \langle Q_{LW,clr} \rangle) + \sum_{i=1}^{9} f_i (\langle \overline{Q_{SW,cld_i}} \rangle + \langle \overline{Q_{LW,cld_i}} \rangle) + LE + SH$$

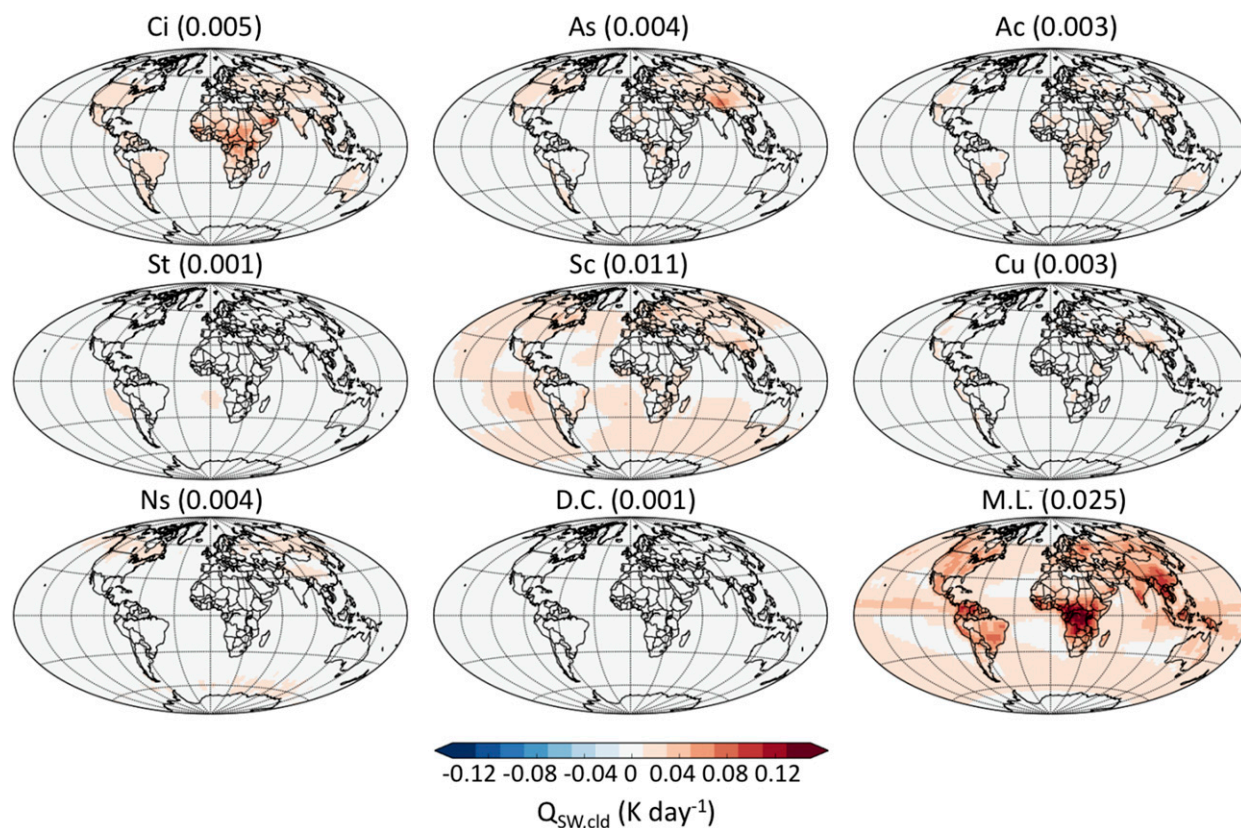$$= Q_{SW,clr} + Q_{LW,clr} + \sum_{i=1}^{9} (Q_{SW,cld_i} + Q_{LW,cld_i}) + LE_{rain} + LE_{snow} + SH, \qquad (3)$$

FIG. 7. As in Fig. 6, but for cloud impact on SW heating (K day^{-1}).

where f_{clr} is the fraction of clear-sky scenes, $\langle Q_{clr} \rangle$ is the conditional mean atmospheric cooling of clear sky. The subscript i, denotes each of the nine cloud types in 2BCLD cloud classification and f_i is the cloud fraction of each cloud type i (Fig. 2). $\langle Q_{cld} \rangle$ is the conditional mean cloud impact. Q_{SW,cld_i} or Q_{LW,cld_i} is defined as the cloud impact on SW (Fig. 7) or LW (Fig. 8) atmospheric heating, weighted by the cloud fraction of each cloud type i. LE_{rain} or LE_{snow} is the amount of latent heat released from rain or snow and SH is sensible heating.

Figure 10 compares the contributions of each term in Eq. (3) to the global annual mean atmospheric heating. In clear skies, the LW cooling is almost 4 times stronger than the SW heating, resulting in a net atmospheric cooling of -1.1 K day^{-1}. Despite covering nearly 70% of the sky on average, however, clouds heat the atmosphere by only 0.07 K day^{-1}, or about 6% of the clear-sky radiative cooling. Although cirrus, stratocumulus, and multilayered clouds are abundant, they contribute less than 0.05 K day^{-1} to total atmospheric heating when integrated over the globe. This small global mean cloud impact, however, is the result of cancellation of warming and cooling effects of different cloud types in different

regions. Such cancellation does not occur in clear skies where LW radiative cooling dominates or in precipitation where latent heating is always positive. Cloud heating is also much smaller than the latent heat released in precipitation, which is estimated to be 0.66 K day^{-1} derived from GPCP-WALRUS and sensible heat, which is estimated to be 0.15 K day^{-1} derived from ERA-Interim reanalysis.

To emphasize the potential for clouds to impact atmospheric heating regionally, Fig. 11 compares zonal averaged distributions of clear-sky atmospheric cooling, cloud impact on atmospheric heating, and latent heat released from precipitation. Zonal mean cloud impact is greatest at 5°N where it reaches 0.3 K day^{-1}, canceling nearly a quarter of clear-sky radiative cooling. In the polar regions, clouds cool the atmosphere efficiently offsetting all latent heat release poleward of 70°. The balance between radiative cooling and latent heating has been shown to be an important control on precipitation (Stephens and Ellis 2008). These comparisons reveal that cloud impacts can play an important role in defining this balance zonally with potentially important implications for the general circulation (Slingo and Slingo 1988).
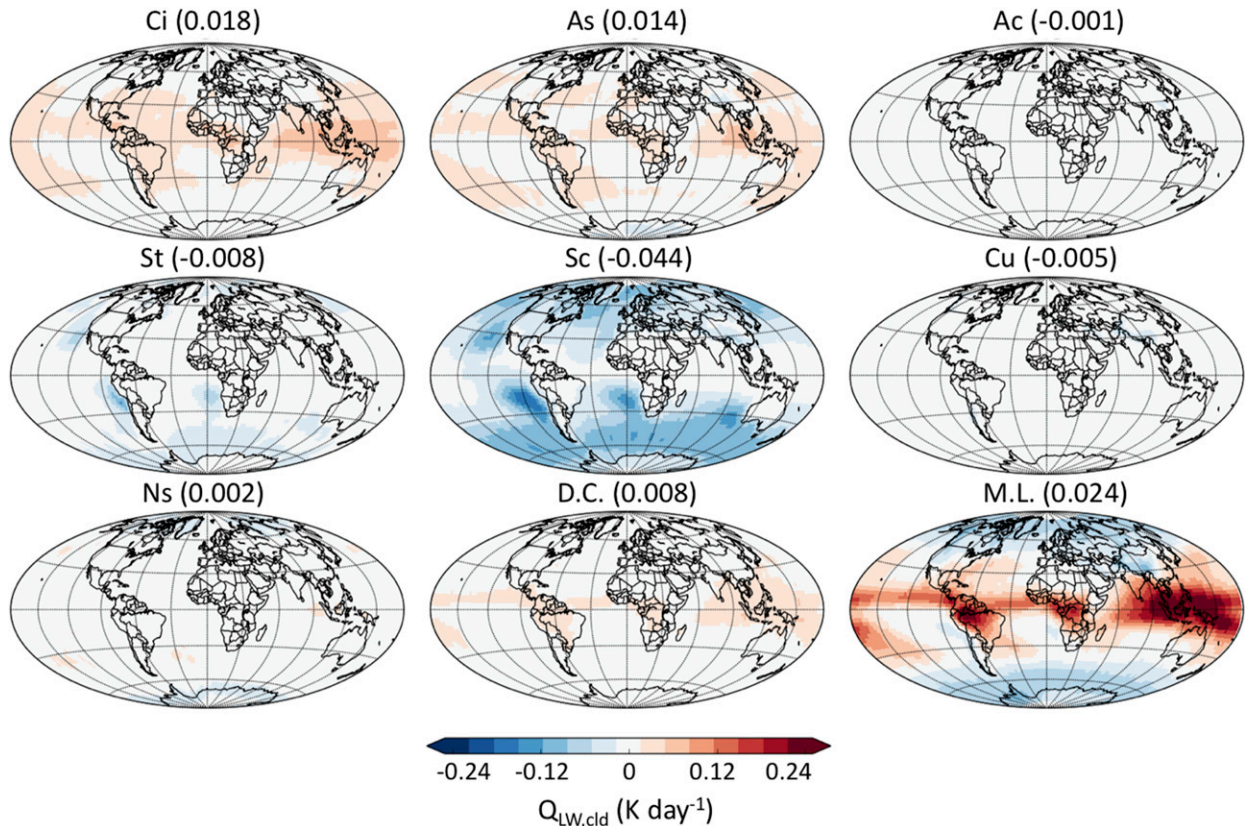
FIG. 8. As in Fig. 6, but for cloud impact on LW heating (K day^{-1}).

These strong zonal variations in cloud impacts can, of course, be traced to regional variations in the occurrence of different cloud types. Figure 12 decomposes atmospheric radiative heating in four broad latitude bands into contributions from clear skies and each observed cloud type. Clear-sky atmospheric cooling decreases from tropics to the poles due to the colder emitting temperatures and reduction in LW cooling from water vapor. By contrast, cloud impacts exhibit more regional diversity ranging from net heating in the tropics (0.23 K day^{-1}) to net cooling in the poles (-0.13 K day^{-1}). The regional diversity coincides with large variations in cloud type. Interestingly, in all but the midlatitude band, the largest contribution to the cloud impact is provided by multilayered cloud systems, which act to heat the tropics but cool the poles primarily through their influences on LW radiation. By contrast, cirrus clouds cause atmospheric LW heating from the equator to the pole, while stratocumulus clouds increase atmospheric LW cooling at all latitudes, dominating the overall cloud impact on atmospheric heating in the midlatitudes. When considered in the context of the global atmospheric heat transport, these results demonstrate that clouds significantly enhance meridional heating

gradients consistent with the suggested two-way coupling between clouds and atmospheric circulations (Hartmann and Short 1980; Slingo and Slingo 1991; Li et al. 2015; Harrop and Hartmann 2016; Winker et al. 2017).
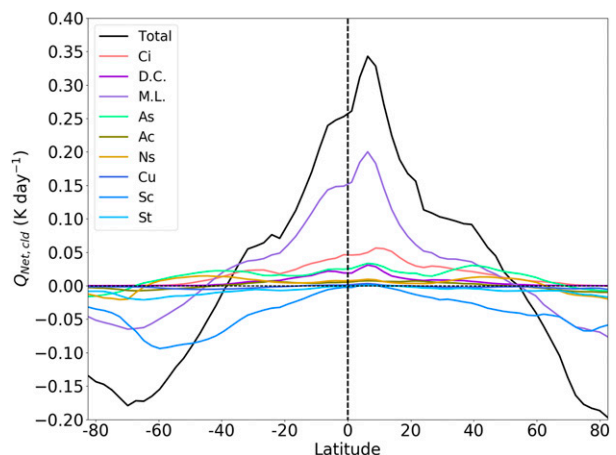

FIG. 9. Zonal mean impact of each cloud type on zonal–annual mean net atmospheric radiative heating (K day^{-1}). Cloud types are determined based on 2B-CLDCLASS-lidar cloud classification.
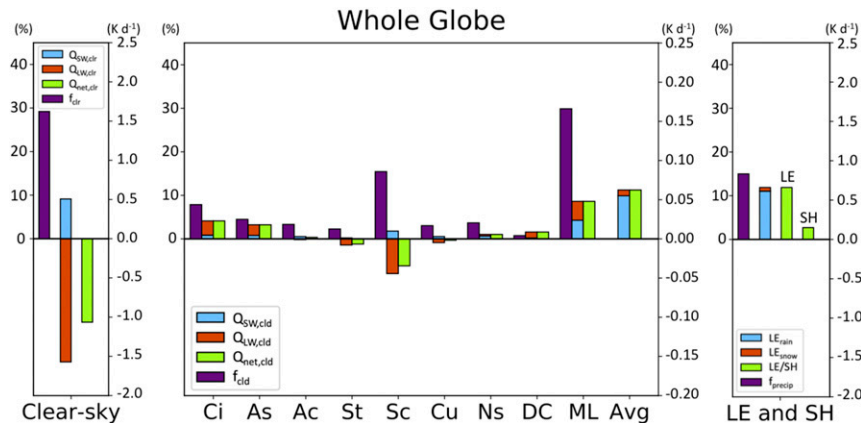
FIG. 10. Global decomposition of net atmospheric heating into its sources (K day^{-1}). (left) The global mean fraction of clear-sky scenes (purple) and their contribution to SW, LW, and net atmospheric cooling (blue, red, and green, respectively). (middle) Contribution of each 2BCLD cloud type to global atmospheric heating. (right) Global mean latent and sensible heating. Global precipitation fraction (purple) is derived from CloudSat 2C-PRECIP-COLUMN product (Haynes et al. 2009). The global mean latent heating is from GPCP-WALRUS in blue. The small red bar at the top represents an estimate of the fraction of this LE that comes from snow based on the CloudSat 2C-SNOW (7% of the total).

c. Influence of clouds on hemispheric heating imbalances

Hemispheric energy imbalances and the resulting cross-equatorial heat transport play a key role in establishing the location of the region of large-scale ascending branch of the meridional overturning circulation, or ITCZ, and the associated global precipitation maximum (Donohoe et al. 2013; Hwang and Frierson 2013; Frierson et al. 2013; Loeb et al. 2016; Stephens et al. 2016). Figure 9 clearly indicates that clouds play a role in setting the hemispheric energy imbalances as cloud impacts on atmospheric heating are decidedly asymmetric about the equator. Clouds cool more strongly in the southern high latitudes while the peak in tropical cloud heating resides with the ITCZ north of the equator. The asymmetry in cloud heating is more directly quantified in Fig. 13 where column-integrated impact of clouds in the Northern Hemisphere and Southern Hemisphere (SH) are summarized separately. Overall cloud heating is 3 times stronger in the NH (0.1 ± 0.08 K day^{-1} or 3.1 ± 2.5 PW) than in the SH (0.04 ± 0.08 K day^{-1} or 1.1 ± 2.5 PW). As a result, clouds induce a substantial 1.4 PW (shown in Fig. 14, the difference of hemispheric imbalance in Q_{cld} and LE) of atmospheric heat transport (approximately two-thirds of the total heating asymmetry of 2.0 ± 3.5 PW) from the SH to the NH relative to cloud free skies. The decomposition into cloud types presented here support previous assertions that in addition to tropical cloud effects, remote influences from extratropical clouds

contribute to this imbalance (e.g., Yoshimori and Broccoli 2008; Frierson and Hwang 2012). Figure 13 indicates that enhanced LW cooling by stratocumulus clouds over the Southern Ocean and excess LW heating from multilayered clouds in the Northern Hemisphere each contribute approximately one-third of this asymmetry. In both cases, cloud impacts on longwave radiation are primarily responsible for the asymmetry. More frequent stratocumulus clouds over the southern oceans increase downwelling LW radiation from the atmosphere to the surface, enhancing atmospheric cooling in the SH relative to the NH storm tracks. Conversely, enhanced upper-level cloud cover associated with the
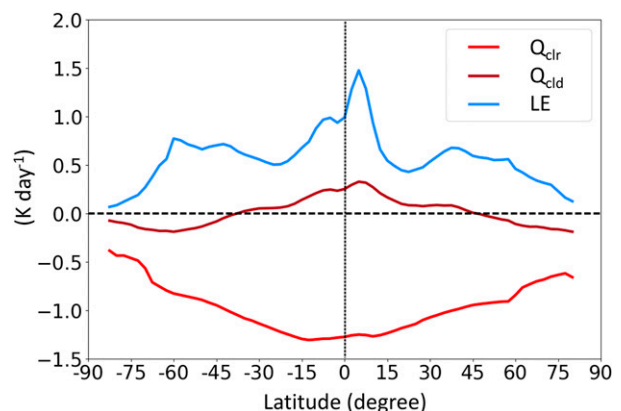

FIG. 11. Zonal mean Q_{clr}, Q_{cld}, and LE (K day^{-1}). Q_{clr} and Q_{cld} are calculated by 2B-FLXHR-lidar. LE is calculated using the combination of GPCP and WALRUS.
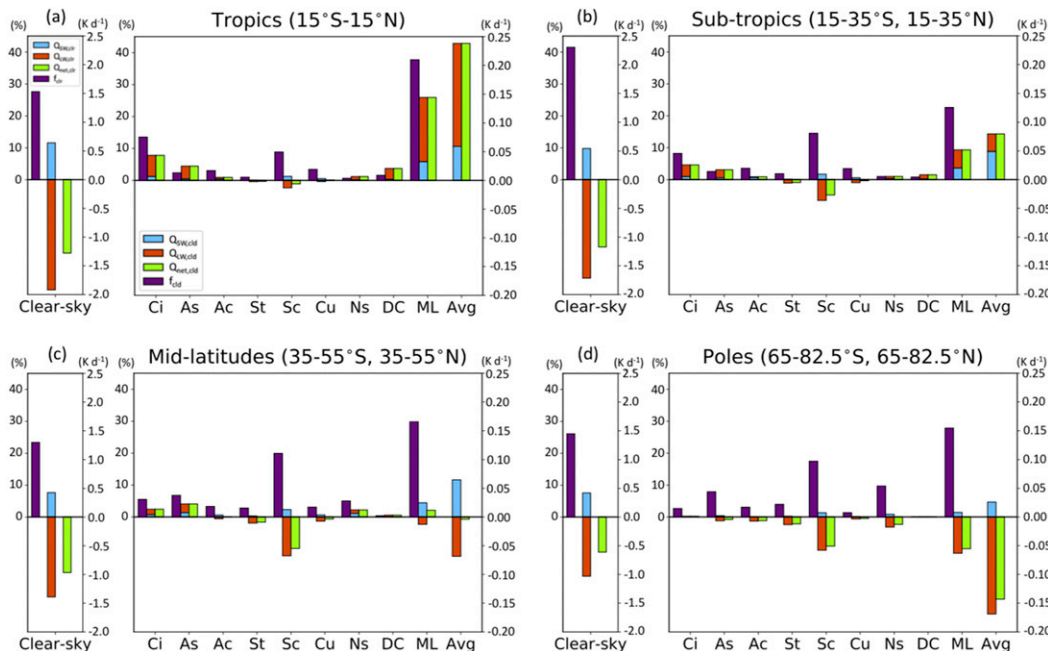
FIG. 12. As in Fig. 10, but for four latitude bands: (a) tropics, (b) subtropics, (c) midlatitudes, and (d) poles (K day^{-1}).

asymmetric location of the ITCZ in the Northern Hemisphere leads to an enhanced greenhouse effect that amplifies this hemispheric imbalance.

Figure 14 compares the magnitudes of these estimates of cloud-induced hemispheric atmospheric heating imbalances against corresponding imbalances in clear-sky atmospheric cooling, latent heat released in precipitation, and sensible heat exchanges between the surface and the atmosphere. While cloud impacts on atmospheric heating only amount to about 10% of Q_{clr} and LE on the global mean (Fig. 10), hemispheric asymmetries in cloud heating are larger than those in either clear-sky atmospheric cooling and latent heat. In fact, the hemispheric asymmetry in cloud impacts on atmospheric heating is larger than the other three sources combined. This suggests that hemispheric imbalances in cloud heating, that include both remote influences and those associated with high clouds in the ITCZ itself, play an important role in reinforcing the present-day Northern Hemisphere location of the ITCZ and associated tropical precipitation maximum. Furthermore, the decomposition of this cloud-induced hemispheric atmospheric energy imbalance into components from distinct cloud types supports the assertion that a relatively small bias in SH cloud cover could influence the predicted location of the ITCZ (Hwang and Frierson 2013). Figures 13 and 14 thus provide references against which the simulated impacts of distinct cloud types on hemispheric energy imbalances in

reanalysis and coupled global models may be compared (Trenberth and Fasullo 2010).

As noted in prior studies, cloud radiative effects over the Southern Ocean exhibit a strong seasonal cycle (Rossow and Lacis 1990; Klein and Hartmann 1993; Trenberth and Fasullo 2010; Haynes et al. 2011). As a result, much of the observed asymmetry in cloud heating impacts can be traced to the SH winter months when solar insolation is at a minimum placing a greater

Global	Ci	As	Ac	St	Sc	Cu	Ns	D.C.	M.L.	Total
CF	7.9	4.5	3.3	2.3	15.5	3.0	3.7	0.8	29.9	70.8
$Q_{SW,cld}$	0.005	0.004	0.003	0.001	0.011	0.003	0.004	0.001	0.025	0.06
$Q_{LW,cld}$	0.018	0.014	-0.001	-0.008	-0.044	-0.005	0.002	0.008	0.024	0.01
$Q_{Net,cld}$	0.023	0.018	0.002	-0.007	-0.033	-0.002	0.006	0.009	0.049	0.07
NH										
CF	9.1	5.1	3.5	1.5	12.3	3.0	3.4	0.9	30.5	69.3
$Q_{SW,cld}$	0.007	0.006	0.004	0.001	0.010	0.004	0.004	0.001	0.030	0.07
$Q_{LW,cld}$	0.020	0.014	-0.001	-0.005	-0.032	-0.005	0.001	0.009	0.029	0.03
$Q_{Net,cld}$	0.028	0.020	0.003	-0.004	-0.022	-0.001	0.005	0.010	0.059	0.10
SH										
CF	6.7	3.9	3.2	3.1	18.6	3.1	4.0	0.6	29.3	72.4
$Q_{SW,cld}$	0.003	0.003	0.002	0.002	0.011	0.002	0.003	0.001	0.020	0.05
$Q_{LW,cld}$	0.016	0.013	-0.001	-0.010	-0.056	-0.005	0.003	0.007	0.019	-0.01
$Q_{Net,cld}$	0.019	0.016	0.001	-0.008	-0.045	-0.003	0.006	0.008	0.039	0.04
NH-SH										
CF	2.4	1.2	0.3	-1.6	-6.3	-0.1	-0.6	0.3	1.2	-3.1
$Q_{SW,cld}$	0.004	0.003	0.002	-0.001	-0.001	0.002	0.001	0.000	0.010	0.02
$Q_{LW,cld}$	0.004	0.001	0.000	0.005	0.024	0.000	-0.002	0.002	0.010	0.04
$Q_{Net,cld}$	0.008	0.004	0.002	0.004	0.023	0.002	-0.001	0.002	0.020	0.06

FIG. 13. Influence of vertical structure-based cloud types on global, Northern Hemisphere, and Southern Hemisphere annual mean column-integrated atmospheric radiative heating (K day^{-1}). The global fraction of each cloud type, CF (%), is reported in top row.

	$Q_{SW,cld}$	$Q_{LW,cld}$	$Q_{Net,cld}$	$Q_{SW,clr}$	$Q_{LW,clr}$	$Q_{Net,clr}$	LE	SH
Global	0.06	0.01	0.07	0.51	-1.57	-1.07	0.66	0.15±0.01
(PW)	3.5	0.5	3.9	31.2	-96.2	-65.2	40.3	9.2±0.7
NH	0.07	0.03	0.10	0.52	-1.59	-1.07	0.67	0.17±0.01
(PW)	2.2	0.9	3.1	15.9	-48.6	-32.6	20.5	5.2±0.3
SH	0.05	-0.01	0.04	0.49	-1.56	-1.06	0.65	0.12±0.01
(PW)	1.5	-0.4	1.1	15.1	-47.7	-32.5	19.8	3.7±0.4
NH-SH	0.02	0.04	0.06	0.03	-0.03	-0.01	0.02	0.05±0.01
(PW)	0.7	1.3	2.0	0.8	-0.9	-0.1	0.6	1.5±0.2

FIG. 14. Hemispheric differences in cloud impact on atmospheric radiative heating, Q_{cld}, clear-sky atmospheric radiative heating, Q_{clr}, atmospheric latent heating, LE, and sensible heating (K day^{-1}). Q_{clr} and Q_{cld} are derived from 2BFLX, and q is derived from the GPCP and WALRUS while SH is estimated from ERA-Interim reanalysis (error bars are derived from standard deviation of ERA-Interim, JRA-55, MERRA, and MERRA-2). All the values are also reported in PW.

emphasis on the longwave radiative cooling effects of the stratocumulus clouds over the southern oceans. Figure 15 contrasts the annual cycles of cloud impacts on atmospheric heating in each hemisphere. Global Q_{cld} as well as its SW and LW components are approximately constant throughout the year. Cloud heating in each hemisphere, however, tracks the annual progression of the sun from the SH in December, January, and February to the NH in June, July, and August. Variations in SW heating are largely symmetric between the hemispheres peaking in the summer hemisphere, but the peak LW cloud heating in the NH summer is considerably stronger than in the SH and remains above the global mean for more than eight months of the year. When combined with the reinforcing effects of a stronger atmospheric greenhouse effect in the NH tropics, this causes the hemispheric imbalance in cloud heating to reach a maximum in the SH winter. When combined with $Q_{SW,cld}$, the hemispheric imbalance of $Q_{Net,cld}$ reaches a peak of 0.24 K day^{-1} (or 7.3 PW) in July (Fig. 15a).

4. Discussion and conclusions

This work documents the influences of nine vertical-structure-based cloud types on atmospheric radiative heating using *CloudSat* and *CALIPSO* observations. On the global annual mean, clouds induce a net planetary atmospheric radiative heating of 0.07 ± 0.08 K day^{-1} (0.06 ± 0.07 K day^{-1} in the SW, 0.01 ± 0.04 K day^{-1} in the LW). Multilayered cloud systems, which are ubiquitous in both hemispheres, are found to exert the strongest influence on the global atmospheric heating. About two-thirds of the heating from multilayer clouds is, however, offset by enhanced cooling from stratocumulus clouds that are the most common single-layer cloud type observed. While this leads to a relatively small influence on global, annual mean atmospheric heating (roughly 10% as large as the clear-sky
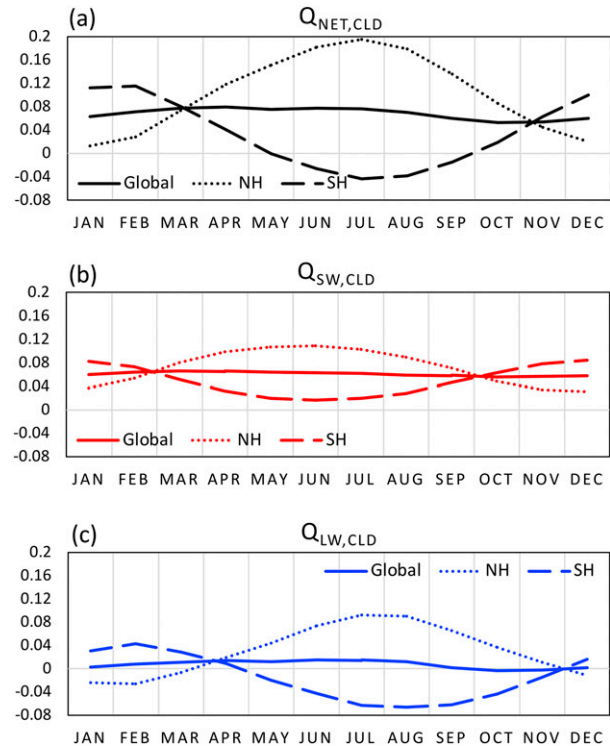

FIG. 15. Annual cycle of (a) $Q_{Net,cld}$, (b) $Q_{SW,cld}$, and (c) $Q_{LW,cld}$ (K day^{-1}). Solid lines represent the global mean while dotted and dashed curves isolate the contributions from the NH and SH, respectively.

cooling and latent heat release in precipitation formation), clouds can exert an influence on zonal-mean atmospheric heating that is comparable to clear-sky atmospheric cooling and latent heat release in some regions. It is found that clouds heat the tropics by 0.23 K day^{-1} and cool the poles by −0.13 K day^{-1}, significantly influencing zonal heat redistribution, and supporting stronger poleward energy fluxes (Harrop and Hartmann 2016).

These zonal variations in cloud heating, in turn, lead to a strong hemispheric asymmetry in atmospheric heating that is driven by both the local effects of multilayered clouds in the ITCZ itself and the remote influence from stratocumulus clouds over the southern oceans. This hemispheric asymmetry in cloud heating peaks in the NH summer when the ITCZ is at its northernmost latitude and the effects of SH stratocumulus are dominated by LW cooling. On the annual mean, clouds heat the NH by 0.1 ± 0.08 K day^{-1}, nearly 3 times stronger than cloud heating in SH (0.04 ± 0.08 K day^{-1}). The resulting 2 ± 3.5 PW imbalance in cloud heating implies that clouds induce more than 1 PW of southward heat transport across the equator relative to clear skies. The decomposition into cloud types presented here suggests that tropical

and extratropical cloud systems contribute approximately equally to this imbalance.

The magnitude of the cloud-induced atmospheric hemispheric energy imbalance inferred from *CloudSat* and *CALIPSO* observations lies at the upper bound of the total southward atmospheric heat transport (0.33 ± 0.6 PW) estimated by Stephens et al. (2016). One reason for this discrepancy may be that the CERES Energy Balance and Filled (EBAF) product underestimates downwelling longwave radiation (DLR) by several $W\,m^{-2}$ relative to similar products that include active sensor information such as 2BFLX and the CERES-*CloudSat*-*CALIPSO*-MODIS (C3M) product (Kato et al. 2012; Stephens et al. 2012a; Ham et al. 2017). Since Part I demonstrated that cloud impacts on DLR are $4.3\,W\,m^{-2}$ larger in the SH, primarily from stratocumulus clouds over the southern oceans, it is plausible that this key source of SH atmospheric cooling is stronger in 2BFLX than EBAF. While there are reasons to believe that active sensors may improve estimates of downwelling fluxes (Stephens et al. 2012a; Henderson et al. 2013; Mülmenstädt et al. 2018), the precise magnitude of cloud impact on DLR in the SH is difficult to estimate and remains uncertain at this time as captured by the large error bars in both the present work and Stephens et al. (2016). However, it is clear that even a small increase in SH downwelling LW radiation of a few $W\,m^{-2}$ induces a significant shift in the estimated partitioning of cross-equatorial heat transport from the oceans to the atmosphere.

REFERENCES

Austin, R., 2007: Level 2b radar-only cloud water content (2B-CWC-RO) process description document. CloudSat Project Rep. 5, 26 pp., ftp://ftp.cira.colostate.edu/ftp/CloudSat/Docs/2B-CWC-RO_PDICD.P_R04.20071021.pdf.

——, A. J. Heymsfield, and G. L. Stephens, 2009: Retrieval of ice cloud microphysical parameters using the CloudSat millimeter-wave radar and temperature. *J. Geophys. Res.*, **114**, D00A23, https://doi.org/10.1029/2008JD010049.

Cesana, G., D. Waliser, D. Henderson, T. L'Ecuyer, X. Jiang, and J.-L. Li, 2019: The vertical structure of radiative heating rates: A multimodel evaluation using A-Train satellite observations. *J. Climate*, **32**, 1573–1590, https://doi.org/10.1175/JCLI-D-17-0136.1.

Chan, M. A., and J. C. Comiso, 2011: Cloud features detected by MODIS but not by CloudSat and CALIOP. *Geophys. Res. Lett.*, **38**, L24813, https://doi.org/10.1029/2011GL050063.

Chen, T., W. B. Rossow, and Y. Zhang, 2000: Radiative effects of cloud-type variations. *J. Climate*, **13**, 264–286, https://doi.org/10.1175/1520-0442(2000)013<0264:REOCTV>2.0.CO;2.

Deng, M., G. G. Mace, Z. Wang, and R. P. Lawson, 2013: Evaluation of several A-Train ice cloud retrieval products with in situ measurements collected during the SPARTICUS campaign. *J. Appl. Meteor. Climatol.*, **52**, 1014–1030, https://doi.org/10.1175/JAMC-D-12-054.1.

Donohoe, A., J. Marshall, D. Ferreira, and D. Mcgee, 2013: The relationship between ITCZ location and cross-equatorial atmospheric heat transport: From the seasonal cycle to the last glacial maximum. *J. Climate*, **26**, 3597–3618, https://doi.org/10.1175/JCLI-D-12-00467.1.

Frierson, D. M., and Y.-T. Hwang, 2012: Extratropical influence on ITCZ shifts in slab ocean simulations of global warming. *J. Climate*, **25**, 720–733, https://doi.org/10.1175/JCLI-D-11-00116.1.

——, and Coauthors, 2013: Contribution of ocean overturning circulation to tropical rainfall peak in the Northern Hemisphere. *Nat. Geosci.*, **6**, 940–944, https://doi.org/10.1038/NGEO1987.

Fueglistaler, S., A. Dessler, T. Dunkerton, I. Folkins, Q. Fu, and P. W. Mote, 2009: Tropical tropopause layer. *Rev. Geophys.*, **47**, RG1004, https://doi.org/10.1029/2008RG000267.

Ham, S.-H., and Coauthors, 2017: Cloud occurrences and cloud radiative effects (CRES) from CERES-CALIPSO-CloudSat-MODIS (CCCM) and CloudSat radar-lidar (RL) products. *J. Geophys. Res. Atmos.*, **122**, 8852–8884, https://doi.org/10.1002/2017JD026725.

Harrop, B. E., and D. L. Hartmann, 2016: The role of cloud radiative heating in determining the location of the ITCZ in aquaplanet simulations. *J. Climate*, **29**, 2741–2763, https://doi.org/10.1175/JCLI-D-15-0521.1.

Hartmann, D. L., and D. A. Short, 1980: On the use of earth radiation budget statistics for studies of clouds and climate. *J. Atmos. Sci.*, **37**, 1233–1250, https://doi.org/10.1175/1520-0469(1980)037<1233:OTUOER>2.0.CO;2.

Haynes, J. M., T. S. L'Ecuyer, G. L. Stephens, S. D. Miller, C. Mitrescu, N. B. Wood, and S. Tanelli, 2009: Rainfall retrieval over the ocean with spaceborne W-band radar. *J. Geophys. Res.*, **114**, D00A22, https://doi.org/10.1029/2008JD009973.

——, C. Jakob, W. B. Rossow, G. Tselioudis, and J. Brown, 2011: Major characteristics of Southern Ocean cloud regimes and their effects on the energy budget. *J. Climate*, **24**, 5061–5080, https://doi.org/10.1175/2011JCLI4052.1.

——, T. H. Vonder Haar, T. L'Ecuyer, and D. Henderson, 2013: Radiative heating characteristics of Earth's cloudy atmosphere from vertically resolved active sensors. *Geophys. Res. Lett.*, **40**, 624–630, https://doi.org/10.1002/grl.50145.

Henderson, D. S., T. L'Ecuyer, G. Stephens, P. Partain, and M. Sekiguchi, 2013: A multisensor perspective on the radiative impacts of clouds and aerosols. *J. Appl. Meteor. Climatol.*, **52**, 853–871, https://doi.org/10.1175/JAMC-D-12-025.1.

Huang, X., X. Chen, D. K. Zhou, and X. Liu, 2016: An observationally based global band-by-band surface emissivity dataset for climate and weather simulations. *J. Atmos. Sci.*, **73**, 3541–3555, https://doi.org/10.1175/JAS-D-15-0355.1.

Huffman, G. J., and Coauthors, 1997: The Global Precipitation Climatology Project (GPCP) combined precipitation dataset.

Bull. Amer. Meteor. Soc., **78**, 5–20, https://doi.org/10.1175/1520-0477(1997)078<0005:TGPCPG>2.0.CO;2.

Hwang, Y.-T., and D. M. Frierson, 2013: Link between the double-intertropical convergence zone problem and cloud biases over the Southern Ocean. *Proc. Natl. Acad. Sci. USA*, **110**), 4935–4940, https://doi.org/10.1073/pnas.1213302110.

Jakub, F., and B. Mayer, 2015: A three-dimensional parallel radiative transfer model for atmospheric heating rates for use in cloud resolving models—The *TenStream* solver. *J. Quant. Spectrosc. Radiat. Transfer*, **163**, 63–71, https://doi.org/10.1016/j.jqsrt.2015.05.003.

Jiang, X., and Coauthors, 2015: Vertical structure and physical processes of the Madden–Julian oscillation: Exploring key model physics in climate simulations. *J. Geophys. Res.*, **120**, 4718–4748, https://doi.org/10.1002/2014JD022375.

Jin, Z., Y. Qiao, Y. Wang, Y. Fang, and W. Yi, 2011: A new parameterization of spectral and broadband ocean surface albedo. *Opt. Express*, **19**, 26 429–26 443, https://doi.org/10.1364/OE.19.026429.

Johansson, E., A. Devasthale, T. L'Ecuyer, A. M. Ekman, and M. Tjernström, 2015: The vertical structure of cloud radiative heating over the Indian subcontinent during summer monsoon. *Atmos. Chem. Phys.*, **15**, 11 557–11 570, https://doi.org/10.5194/acp-15-11557-2015.

Johnson, R. H., and G. S. Young, 1983: Heat and moisture budgets of tropical mesoscale anvil clouds. *J. Atmos. Sci.*, **40**, 2138–2147, https://doi.org/10.1175/1520-0469(1983)040<2138:HAMBOT>2.0.CO;2.

Kato, S., F. G. Rose, and T. P. Charlock, 2005: Computation of domain-averaged irradiance using satellite-derived cloud properties. *J. Atmos. Oceanic Technol.*, **22**, 146–164, https://doi.org/10.1175/JTECH-1694.1.

——, S. Sun-Mack, W. F. Miller, F. G. Rose, Y. Chen, P. Minnis, and B. A. Wielicki, 2010: Relationships among cloud occurrence frequency, overlap, and effective thickness derived from CALIPSO and CloudSat merged cloud vertical profiles. *J. Geophys. Res.*, **115**, D00H28, https://doi.org/10.1029/2009JD012277.

——, N. G. Loeb, D. A. Rutan, F. G. Rose, S. Sun-Mack, W. F. Miller, and Y. Chen, 2012: Uncertainty estimate of surface irradiances computed with MODIS-, CALIPSO-, and CloudSat-derived cloud and aerosol properties. *Surv. Geophys.*, **33**, 395–412, https://doi.org/10.1007/s10712-012-9179-x.

Klein, S. A., and D. L. Hartmann, 1993: The seasonal cycle of low stratiform clouds. *J. Climate*, **6**, 1587–1606, https://doi.org/10.1175/1520-0442(1993)006<1587:TSCOLS>2.0.CO;2.

L'Ecuyer, T. S., and G. L. Stephens, 2003: The tropical oceanic energy budget from the TRMM perspective. Part I: Algorithm and uncertainties. *J. Climate*, **16**, 1967–1985, https://doi.org/10.1175/1520-0442(2003)016<1967:TTOEBF>2.0.CO;2.

——, and J. H. Jiang, 2010: Touring the atmosphere aboard the A-Train. *Phys. Today*, **63**, 36–41, https://doi.org/10.1063/1.3463626.

——, N. B. Wood, T. Haladay, G. L. Stephens, and P. W. Stackhouse, 2008: Impact of clouds on atmospheric heating based on the R04 CloudSat fluxes and heating rates data set. *J. Geophys. Res.*, **113**, D00A15, https://doi.org/10.1029/2008JD009951.

——, and Coauthors, 2015: The observed state of the energy budget in the early twenty-first century. *J. Climate*, **28**, 8319–8346, https://doi.org/10.1175/JCLI-D-14-00556.1.

——, Y. Hang, A. V. Matus, and Z. Wang, 2019: Reassessing the effect of cloud type on Earth's energy balance in the age of

active spaceborne observations. Part I: Top of atmosphere and surface. *J. Climate*, **32**, 6197–6217, https://doi.org/10.1175/JCLI-D-18-0753.1.

Li, J.-L., and Coauthors, 2016: Considering the radiative effects of snow on tropical Pacific Ocean radiative heating profiles in contemporary GCMs using A-Train observations. *J. Geophys. Res. Atmos.*, **121**, 1621–1636, https://doi.org/10.1002/2015JD023587.

Li, Y., D. W. Thompson, and S. Bony, 2015: The influence of atmospheric cloud radiative effects on the large-scale atmospheric circulation. *J. Climate*, **28**, 7263–7278, https://doi.org/10.1175/JCLI-D-14-00825.1.

Lin, L., Q. Fu, H. Zhang, J. Su, Q. Yang, and Z. Sun, 2013: Upward mass fluxes in tropical upper troposphere and lower stratosphere derived from radiative transfer calculations. *J. Quant. Spectrosc. Radiat. Transfer*, **117**, 114–122, https://doi.org/10.1016/j.jqsrt.2012.11.016.

Loeb, N. G., H. Wang, A. Cheng, S. Kato, J. T. Fasullo, K.-M. Xu, and R. P. Allan, 2016: Observational constraints on atmospheric and oceanic cross-equatorial heat transports: Revisiting the precipitation asymmetry problem in climate models. *Climate Dyn.*, **46**, 3239–3257, https://doi.org/10.1007/s00382-015-2766-z.

Mace, G. G., and F. J. Wrenn, 2013: Evaluation of the hydrometeor layers in the east and west Pacific within ISCCP cloud-top pressure–optical depth bins using merged *CloudSat* and *CALIPSO* data. *J. Climate*, **26**, 9429–9444, https://doi.org/10.1175/JCLI-D-12-00207.1.

——, and Coauthors, 2006: Cloud radiative forcing at the Atmospheric Radiation Measurement Program Climate Research Facility: 1. Technique, validation, and comparison to satellite-derived diagnostic quantities. *J. Geophys. Res.*, **111**, D11S90, https://doi.org/10.1029/2005JD005921.

——, Q. Zhang, M. Vaughan, R. Marchand, G. Stephens, C. Trepte, and D. Winker, 2009: A description of hydrometeor layer occurrence statistics derived from the first year of merged CloudSat and CALIPSO data. *J. Geophys. Res.*, **114**, D00A26, https://doi.org/10.1029/2007JD009755.

Manabe, S., and F. Möller, 1961: On the radiative equilibrium and heat balance of the atmosphere. *Mon. Wea. Rev.*, **89**, 503–532, https://doi.org/10.1175/1520-0493(1961)089<0503:OTREAH>2.0.CO;2.

——, and R. F. Strickler, 1964: Thermal equilibrium of the atmosphere with a convective adjustment. *J. Atmos. Sci.*, **21**, 361–385, https://doi.org/10.1175/1520-0469(1964)021<0361:TEOTAW>2.0.CO;2.

——, and R. T. Wetherald, 1967: Thermal equilibrium of the atmosphere with a given distribution of relative humidity. *J. Atmos. Sci.*, **24**, 241–259, https://doi.org/10.1175/1520-0469(1967)024<0241:TEOTAW>2.0.CO;2.

Marchand, R., T. Ackerman, M. Smyth, and W. B. Rossow, 2010: A review of cloud top height and optical depth histograms from MISR, ISCCP, and MODIS. *J. Geophys. Res.*, **115**, D16206, https://doi.org/10.1029/2009JD013422.

Matus, A. V., and T. S. L'Ecuyer, 2017: The role of cloud phase in earth's radiation budget. *J. Geophys. Res. Atmos.*, **122**, 2559–2578, https://doi.org/10.1002/2016JD025951.

McFarlane, S. A., J. H. Mather, and T. P. Ackerman, 2007: Analysis of tropical radiative heating profiles: A comparison of models and observations. *J. Geophys. Res.*, **112**, D14218, https://doi.org/10.1029/2006JD008290.

McGill, M. J., M. A. Vaughan, C. R. Trepte, W. D. Hart, D. L. Hlavka, D. M. Winker, and R. Kuehn, 2007: Airborne validation of spatial properties measured by the CALIPSO lidar.

J. Geophys. Res., **112**, D20201, https://doi.org/10.1029/2007JD008768.

McIlhattan, E. A., T. S. L'Ecuyer, and N. B. Miller, 2017: Observational evidence linking Arctic supercooled liquid cloud biases in CESM to snowfall processes. *J. Climate*, **30**, 4477–4495, https://doi.org/10.1175/JCLI-D-16-0666.1.

Mülmenstädt, J., and Coauthors, 2018: Using CALIOP to estimate cloud-field base height and its uncertainty: The Cloud Base Altitude Spatial Extrapolator (CBASE) algorithm and dataset. *Earth Syst. Sci. Data*, **10**, 2279–2293, https://doi.org/10.5194/essd-10-2279-2018.

Nelson, E. L., and T. S. L'Ecuyer, 2018: Global character of latent heat release in oceanic warm rain systems. *J. Geophys. Res. Atmos.*, **123**, 4797–4817, https://doi.org/10.1002/2017JD027844.

——, ——, S. M. Saleeby, W. Berg, S. R. Herbener, and S. C. van den Heever, 2016: Toward an algorithm for estimating latent heat release in warm rain systems. *J. Atmos. Oceanic Technol.*, **33**, 1309–1329, https://doi.org/10.1175/JTECH-D-15-0205.1.

Oreopoulos, L., and W. Rossow, 2011: The cloud radiative effects of International Satellite Cloud Climatology Project weather states. *J. Geophys. Res.*, **116**, D12202, https://doi.org/10.1029/2010JD015472.

——, N. Cho, D. Lee, and S. Kato, 2016: Radiative effects of global MODIS cloud regimes. *J. Geophys. Res.*, **121**, 2299–2317, https://doi.org/10.1002/2015JD024502.

——, ——, and ——, 2017: New insights about cloud vertical structure from *CloudSat* and CALIPSO observations. *J. Geophys. Res. Atmos.*, **122**, 9280–9300, https://doi.org/10.1002/2017JD026629.

Platnick, S., M. D. King, S. A. Ackerman, W. P. Menzel, B. A. Baum, J. C. Riedi, and R. A. Frey, 2003: The MODIS cloud products: Algorithms and examples from *Terra. IEEE Trans. Geosci. Remote Sens.*, **41**, 459–473, https://doi.org/10.1109/TGRS.2002.808301.

Protat, A., and Coauthors, 2014: Reconciling ground-based and space-based estimates of the frequency of occurrence and radiative effect of clouds around Darwin, Australia. *J. Appl. Meteor. Climatol.*, **53**, 456–478, https://doi.org/10.1175/JAMC-D-13-072.1.

Ramanathan, V., 1987: The role of earth radiation budget studies in climate and general circulation research. *J. Geophys. Res.*, **92**, 4075–4095, https://doi.org/10.1029/JD092iD04p04075.

Randall, D. A., D. A. Dazlich, and T. G. Corsetti, 1989: Interactions among radiation, convection, and large-scale dynamics in a general circulation model. *J. Atmos. Sci.*, **46**, 1943–1970, https://doi.org/10.1175/1520-0469(1989)046<1943:IARCAL>2.0.CO;2.

Ritter, B., and J.-F. Geleyn, 1992: A comprehensive radiation scheme for numerical weather prediction models with potential applications in climate simulations. *Mon. Wea. Rev.*, **120**, 303–325, https://doi.org/10.1175/1520-0493(1992)120<0303:ACRSFN>2.0.CO;2.

Rossow, W. B., and A. A. Lacis, 1990: Global, seasonal cloud variations from satellite radiance measurements. Part II: Cloud properties and radiative effects. *J. Climate*, **3**, 1204–1253, https://doi.org/10.1175/1520-0442(1990)003<1204:GSCVFS>2.0.CO;2.

——, and Y.-C. Zhang, 1995: Calculation of surface and top of atmosphere radiative fluxes from physical quantities based on ISCCP data sets: 2. validation and first results. *J. Geophys. Res.*, **100**, 1167–1197, https://doi.org/10.1029/94JD02746.

——, and R. A. Schiffer, 1999: Advances in understanding clouds from ISCCP. *Bull. Amer. Meteor. Soc.*, **80**, 2261–2287, https://doi.org/10.1175/1520-0477(1999)080<2261:AIUCFI>2.0.CO;2.

Sabatini, R. R., and V. E. Suomi, 1962: On the possibility of atmospheric infrared cooling estimates from satellite observations. *J. Atmos. Sci.*, **19**, 349–350, https://doi.org/10.1175/1520-0469(1962)019<0349:OTPOAI>2.0.CO;2.

Saleeby, S. M., and W. R. Cotton, 2004: A large-droplet mode and prognostic number concentration of cloud droplets in the Colorado State University Regional Atmospheric Modeling System (RAMS). Part I: Module descriptions and supercell test simulations. *J. Appl. Meteor.*, **43**, 182–195, https://doi.org/10.1175/1520-0450(2004)043<0182:ALMAPN>2.0.CO;2.

——, and S. C. van den Heever, 2013: Developments in the CSU-RAMS aerosol model: Emissions, nucleation, regeneration, deposition, and radiation. *J. Appl. Meteor. Climatol.*, **52**, 2601–2622, https://doi.org/10.1175/JAMC-D-12-0312.1.

Sassen, K., and Z. Wang, 2008: Classifying clouds around the globe with the CloudSat radar: 1-year of results. *Geophys. Res. Lett.*, **35**, L04805, https://doi.org/10.1029/2007GL032591.

——, and ——, 2012: The clouds of the middle troposphere: Composition, radiative impact, and global distribution. *Surv. Geophys.*, **33**, 677–691, https://doi.org/10.1007/s10712-011-9163-x.

——, ——, and D. Liu, 2008: Global distribution of cirrus clouds from CloudSat/Cloud-Aerosol Lidar and Infrared Pathfinder Satellite Observations (CALIPSO) measurements. *J. Geophys. Res.*, **113**, D00A12, https://doi.org/10.1029/2008JD009972.

Slingo, A., and J. Slingo, 1988: The response of a general circulation model to cloud longwave radiative forcing. I: Introduction and initial experiments. *Quart. J. Roy. Meteor. Soc.*, **114**, 1027–1062, https://doi.org/10.1002/qj.49711448209.

Slingo, J., and A. Slingo, 1991: The response of a general circulation model to cloud longwave radiative forcing. II: Further studies. *Quart. J. Roy. Meteor. Soc.*, **117**, 333–364, https://doi.org/10.1002/qj.49711749805.

Soden, B. J., and I. M. Held, 2006: An assessment of climate feedbacks in coupled ocean–atmosphere models. *J. Climate*, **19**, 3354–3360, https://doi.org/10.1175/JCLI3799.1.

Sohn, B.-J., and E. A. Smith, 1992: The significance of cloud–radiative forcing to the general circulation on climate time scales—A satellite interpretation. *J. Atmos. Sci.*, **49**, 845–860, https://doi.org/10.1175/1520-0469(1992)049<0845:TSOCFT>2.0.CO;2.

Stephens, G. L., 2005: Cloud feedbacks in the climate system: A critical review. *J. Climate*, **18** 237–273, https://doi.org/10.1175/JCLI-3243.1.

——, and T. D. Ellis, 2008: Controls of global-mean precipitation increases in global warming GCM experiments. *J. Climate*, **21**, 6141–6155, https://doi.org/10.1175/2008JCLI2144.1.

——, and T. L'Ecuyer, 2015: The earth's energy balance. *Atmos. Res.*, **166**, 195–203, https://doi.org/10.1016/j.atmosres.2015.06.024.

——, and Coauthors, 2002: The *CloudSat* mission and the A-Train: A new dimension of space-based observations of clouds and precipitation. *Bull. Amer. Meteor. Soc.*, **83**, 1771–1790, https://doi.org/10.1175/BAMS-83-12-1771.

——, and Coauthors, 2008: CloudSat mission: Performance and early science after the first year of operation. *J. Geophys. Res.*, **113**, D00A18, https://doi.org/10.1029/2008JD009982.

——, M. Wild, P. W. Stackhouse Jr., T. L'Ecuyer, S. Kato, and D. S. Henderson, 2012a: The global character of the flux of downward longwave radiation. *J. Climate*, **25** 2329–2340, https://doi.org/10.1175/JCLI-D-11-00262.1.

——, and Coauthors, 2012b: An update on Earth's energy balance in light of the latest global observations. *Nat. Geosci.*, **5**, 691–696, https://doi.org/10.1038/ngeo1580.

——, M. Z. Hakuba, M. Hawcroft, J. M. Haywood, A. Behrangi, J. E. Kay, and P. J. Webster, 2016: The curious nature of the hemispheric symmetry of the earth's water and energy balances. *Curr. Climate Change Rep.*, **2** 135–147, https://doi.org/10.1007/s40641-016-0043-9.

Su, H., and Coauthors, 2013: Diagnosis of regime-dependent cloud simulation errors in CMIP5 models using "A-Train" satellite observations and reanalysis data. *J. Geophys. Res.*, **118**, 2762–2780, https://doi.org/10.1029/2012JD018575.

Tanelli, S., S. L. Durden, E. Im, K. S. Pak, D. G. Reinke, P. Partain, J. M. Haynes, and R. T. Marchand, 2008: CloudSat's cloud profiling radar after two years in orbit: Performance, calibration, and processing. *IEEE Trans. Geosci. Remote Sens.*, **46**, 3560–3573, https://doi.org/10.1109/TGRS.2008.2002030.

Trenberth, K. E., and J. T. Fasullo, 2010: Simulation of present-day and twenty-first-century energy budgets of the southern oceans. *J. Climate*, **23**, 440–454, https://doi.org/10.1175/2009JCLI3152.1.

——, ——, and J. Kiehl, 2009: Earth's global energy budget. *Bull. Amer. Meteor. Soc.*, **90**, 311–324, https://doi.org/10.1175/2008BAMS2634.1.

Van Tricht, K., and Coauthors, 2016: Clouds enhance Greenland ice sheet meltwater runoff. *Nat. Commun.*, **7**, 10266, https://doi.org/10.1038/ncomms10266.

Vonder Haar, T. H., and V. E. Suomi, 1971: Measurements of the earth's radiation budget from satellites during a five-year period. Part I: Extended time and space means. *J. Atmos. Sci.*, **28**, 305–314, https://doi.org/10.1175/1520-0469(1971)028<0305:MOTERB>2.0.CO;2.

Webster, P., and G. Stephens, 1984: Cloud–radiation interaction and the climate problem. *The Global Climate*, J. Houghton, Ed., Cambridge University Press, 63–78.

Wielicki, B. A., B. R. Barkstrom, E. F. Harrison, R. B. Lee III, G. L. Smith, and J. E. Cooper, 1996: Clouds and the Earth's Radiant Energy System (CERES): An Earth observing system experiment. *Bull. Amer. Meteor. Soc.*, **77** 853–868, https://doi.org/10.1175/1520-0477(1996)077<0853:CATERE>2.0.CO;2.

Winker, D. M., J. R. Pelon, and M. P. McCormick, 2003: The CALIPSO mission: Spaceborne lidar for observation of aerosols and clouds. *Proc. SPIE*, **4893**, 1–11, https://doi.org/10.1117/12.466539.

——, W. H. Hunt, and M. J. McGill, 2007: Initial performance assessment of CALIOP. *Geophys. Res. Lett.*, **34**, L19803, https://doi.org/10.1029/2007GL030135.

Winker, D., H. Chepfer, V. Noel, and X. Cai, 2017: Observational constraints on cloud feedbacks: The role of active satellite sensors. *Surv. Geophys.*, **38**, 1483–1508, https://doi.org/10.1007/s10712-017-9452-0.

Yoshimori, M., and A. J. Broccoli, 2008: Equilibrium response of an atmosphere–mixed layer ocean model to different radiative forcing agents: Global and zonal mean response. *J. Climate*, **21**, 4399–4423, https://doi.org/10.1175/2008JCLI2172.1.

Zatko, M. C., and S. G. Warren, 2015: East Antarctic sea ice in spring: Spectral albedo of snow, nilas, frost flowers and slush, and light-absorbing impurities in snow. *Ann. Glaciol.*, **56**, 53–64, https://doi.org/10.3189/2015AoG69A574.

Zelinka, M. D., S. A. Klein, K. E. Taylor, T. Andrews, M. J. Webb, J. M. Gregory, and P. M. Forster, 2013: Contributions of different cloud types to feedbacks and rapid adjustments in CMIP5. *J. Climate*, **26**, 5007–5027, https://doi.org/10.1175/JCLI-D-12-00555.1.

Zhang, Y., W. B. Rossow, A. A. Lacis, V. Oinas, and M. I. Mishchenko, 2004: Calculation of radiative fluxes from the surface to top of atmosphere based on ISCCP and other global data sets: Refinements of the radiative transfer model and the input data. *J. Geophys. Res.*, **109**, D19105, https://doi.org/10.1029/2003JD004457.